Geometric phases arising from strong measurements of weak values

IOP Publishing New J. Phys. 26 (2024) 123004 https://doi.org/10.1088/1367-2630/ad9771

New Journal of Physics
The open access journal at the forefront of physics

Deutsche Physikalische Gesellschaft DPG
IOP Institute of Physics

Published in partnership with: Deutsche Physikalische Gesellschaft and the Institute of Physics

OPEN ACCESS

RECEIVED
16 September 2024

REVISED
18 November 2024

ACCEPTED FOR PUBLICATION
26 November 2024

PUBLISHED
5 December 2024

PAPER

Geometric phases arising from strong measurements of weak values

C Montenegro[1], **M Jara**[1], **J P Marrou**[1,2] **and F De Zela**[1,*]

[1] Departamento de Ciencias, Sección Física Pontificia Universidad Católica del Perú, Lima 15088, Peru
[2] Departamento de Física Aplicada, ICMUV, Universidad de Valencia, Dr Moliner 50, Burjassot E-46100, Spain
[*] Author to whom any correspondence should be addressed.

E-mail: fdezela@pucp.edu.pe

Keywords: geometric phases, weak values, quantum–classical border

Abstract

Geometric phases and weak values (WVs) are two fundamental concepts that were originally introduced in the realm of quantum mechanics. In the course of time, it became clear that the two concepts apply in both the quantum domain and the classical domain. Moreover, the two concepts proved to be intimately connected with one another, as disclosed by Sjöqvist some years ago (Sjöqvist 2006 *Phys. Lett.* A **359** 187). WVs were so named in reference to very weak couplings between a system's observable, e.g. light polarization, and its measuring device, the 'pointer'. However, the actual definition of WVs does not involve the system-pointer coupling strength. We have addressed the strong coupling regime both theoretically and experimentally, thereby obtaining geometric phases out of WVs. We report experimental results as a proof-of-concept, using classical light beams and single-shot images. Our approach applies without essential modifications also to single photons.

1. Introduction

Quantum weak values (WVs) [1] and Berry's geometric phase [2] share a rather curious feature. Despite having been introduced as quantum properties, their first experimental realizations were done using classical light [3, 4]. Cases like these illustrate how some properties, which are often claimed to be genuine quantum features, are in fact common to both quantal and classical phenomena. Coherent superposition and entanglement are further examples [5–14]. In contrast to geometric phases, WVs prompted much debate about their meaning [15–20]; but, nevertheless, they soon found multiple applications [21–31]. Among these applications, there is one that connects WVs and geometric phases. It was proposed by Sjöqvist [32] as a non-standard technique for measuring geometric phases. Standard techniques are based on interferometry and polarimetry [34, 35]. They need phase calibration, which is not required in Sjöqvist's proposal. However, the latter requires the accurate measurement of small shifts caused by weakly coupling the observable of interest with position and momentum of the measuring device, something that might be experimentally even more demanding than phase calibration. It is perhaps for this reason that Sjöqvist's proposal has not been put in practice yet, to the best of our knowledge.

Here we present an alternative approach for measuring geometric phases using WVs. As compared to Sjöqvist's proposal, our approach has at least two advantages: It requires the registration of two positions only, and it is not restricted to weak measurements. We recall that WVs were originally introduced in the context of von Neumann's model of the measurement procedure. Central to this model is a Hamiltonian that describes the joint evolution of a system's observable, $\hat{A}$, and a pointer. The WV of $\hat{A}$ is defined [1] as the following, generally complex number:

$$A_w(i,f) = \frac{\langle f|\hat{A}|i\rangle}{\langle f|i\rangle}. \tag{1}$$

Here, $|i\rangle$ is a pre-selected state and $|f\rangle$ is a post-selected state. These states can be conveniently chosen, in connection with the envisioned task. The joined evolution of system and pointer is ruled by the Hamiltonian $\hat{H} = g\hat{A} \otimes \hat{P}$ that acts on the tensor-product space of system and pointer, $\mathcal{H}_S \otimes \mathcal{H}_P$, whereby $\hat{A}$ acts on $\mathcal{H}_S$ and $\hat{P}$ acts on $\mathcal{H}_P$, while g is a coupling constant.

In the particular case in which $\hat{A}$ is a projector, the geometric phase shows up in A_w. This occurs as follows. Given two non-orthogonal vectors $|A\rangle$ and $|B\rangle$, Pancharatnam's relative phase ϕ_{AB} is defined by

$$e^{i\phi_{AB}} = \frac{\langle B|A\rangle}{|\langle B|A\rangle|}. \tag{2}$$

We recall that Pancharatnam's phase is nontransitive: if $|A\rangle$ is in phase with $|B\rangle$, and $|B\rangle$ is in phase with $|C\rangle$, i.e. $\phi_{AB} = 0 = \phi_{BC}$, it can occur that $\phi_{AC} \neq 0$. In such a case, Pancharatnam's phase equals the geometric phase, which in this case can be defined as

$$\Phi_g = \triangle(A, B, C) \equiv \arg\langle A|C\rangle\langle C|B\rangle\langle B|A\rangle. \tag{3}$$

The geometric phase Φ_g is thus given as the argument of a so-called Bargmann invariant [36], a quantity that is invariant under independent phase changes of the vectors which enter it. Consider now the projector $\widehat{\Pi}_B = |B\rangle\langle B|$. Taking $|A\rangle$ as pre-selected state and $|C\rangle$ as post-selected state, the WV of $\widehat{\Pi}_B$ is given, according to (1), by

$$\Pi_B^w(A, C) = \frac{\langle C|\widehat{\Pi}_B|A\rangle}{\langle C|A\rangle} = \frac{\langle C|B\rangle\langle B|A\rangle}{\langle C|A\rangle}. \tag{4}$$

Multiplication and division of the above equation by $\langle A|C\rangle$ leads to

$$\arg\Pi_B^w(A, C) = \triangle(A, B, C). \tag{5}$$

The above equation establishes a connection between WVs and geometric phases [32]. Generally, consider a state given by a normalized vector $|\psi(s)\rangle$, which evolves along a path $\mathcal{C}$, with initial and final points at $s = s_i$ and $s = s_f$, respectively. The geometric phase for $\mathcal{C}$ is defined by [37]

$$\Phi_g(\mathcal{C}) = \arg\langle\psi(s_i)|\psi(s_f)\rangle + i\int_{s_i}^{s_f}\langle\psi(s)|\frac{\mathrm{d}}{\mathrm{d}s}|\psi(s)\rangle \mathrm{d}s \tag{6}$$

$$= \arg\langle\psi(s_i)|\psi(s_f)\rangle - \mathrm{Im}\int_{s_i}^{s_f}\langle\psi(s)|\dot{\psi}(s)\rangle \mathrm{d}s \equiv \Phi_{\mathrm{P}} - \Phi_{\mathrm{dyn}}, \tag{7}$$

where Φ_{P} is Pancharatnam's relative phase between the initial and final states, and Φ_{dyn} is the so-called dynamical phase. We notice that Φ_g is defined modulo 2π and is invariant under parameter transformations $s \to s'(s)$ as well as under local phase transformations: $|\psi(s)\rangle \to |\tilde{\psi}(s)\rangle = e^{i\alpha(s)}|\psi(s)\rangle$. One can use this invariance to get $\Phi_{\mathrm{dyn}} = 0$, in which case $\Phi_g(\mathcal{C}) = \Phi_{\mathrm{P}}$, and one can then measure Φ_{P} by interferometry.

The curve $\mathcal{C}$ traced out by $|\psi(s)\rangle$ is, by definition [37], a geodesic, whenever

$$\mathcal{L}(\mathcal{C}) = \int_{s_i}^{s_f}\sqrt{\langle\dot{\psi}_\perp(s)|\dot{\psi}_\perp(s)\rangle}\,\mathrm{d}s \tag{8}$$

attains an extremal value along $\mathcal{C}$. In equation (8), the vector $|\dot{\psi}_\perp(s)\rangle$ is the component of $|\dot{\psi}(s)\rangle$ which is orthogonal to $\mathcal{C}$, i.e. $|\dot{\psi}_\perp(s)\rangle = |\dot{\psi}(s)\rangle - |\psi(s)\rangle\langle\psi(s)|\dot{\psi}(s)\rangle$. One can prove that, if $\mathcal{C}$ is a geodesic, then $\Phi_g(\mathcal{C}) = 0$ [37]. Let us next take n states $|\psi_k\rangle$, $k = 1, \ldots, n$, so that any two neighboring states are nonorthogonal. Consider the curve $\mathcal{C}$, formed by $n-1$ geodesic arcs joining the n states. The geometric phase is given by

$$\Phi_g(\mathcal{C}) = \Phi_{\mathrm{P}}(\mathcal{C}) - \Phi_{\mathrm{dyn}}(\mathcal{C}) = \arg\langle\psi_1|\psi_n\rangle - \sum_{k=1}^{n-1}\Phi_{\mathrm{dyn}}^{(k,k+1)}, \tag{9}$$

where $\Phi_{\mathrm{dyn}}^{(k,k+1)}$ is the dynamical phase for the geodesic joining $|\psi_k\rangle$ with $|\psi_{k+1}\rangle$. From equation (9), it readily follows [37] that

$$\Phi_g(\mathcal{C}) = -\arg\langle\psi_1|\psi_2\rangle\langle\psi_2|\psi_3\rangle\ldots\langle\psi_n|\psi_1\rangle = -\sum_{k=2}^{n-1}\triangle(\psi_1, \psi_k, \psi_{k+1}). \tag{10}$$

The geometric phase defined by equation (5) can also be seen as arising from joining the three involved vectors by geodesic arcs. This is referred to as a geodesic triangle. Equations (10) and (5) show that $\arg\Pi^{w}_{\psi_k}(\psi_1,\psi_{k+1})$ is a basic building block of geometric phases. Thus, the phases of the (generally complex) WVs are intimately connected with a geometric phase. We can indeed rewrite $\Phi_g(\mathcal{C})$ in equation (10) as the argument of a product of WVs, all of which involve one and the same pre-selected state $|\psi_1\rangle$, a projector $|\psi_k\rangle\langle\psi_k|$ and a post-selected state $|\psi_{k+1}\rangle$:

$$\Phi_g(\mathcal{C}) = -\arg\left\{\Pi^{w}_{\psi_2}(\psi_1,\psi_3)\,\Pi^{w}_{\psi_3}(\psi_1,\psi_4)\ldots\Pi^{w}_{\psi_{n-1}}(\psi_1,\psi_n)\right\}. \tag{11}$$

It should be clear that all the above definitions and derivations hold for any linear vector space, irrespective of the physical interpretation that is given to the vectors themselves. They may represent quantal or classical states. They may also represent vectorial properties that are neither quantal nor classical, because they can be assigned to both quantal carriers and classical carriers. This is the case when one deals with degrees of freedom such as polarization, optical path and transversal amplitude, which may be assigned to both classical light beams and single photons. In this work, we focus on degrees of freedom of this type.

2. Measurement of the geometric phase via WVs

To explain the basic idea of measuring geometric phases using WVs, let us consider the setup shown in figure 1. It allows us to deal with the aforementioned degrees of freedom: transversal amplitude, polarization (spin) and optical path. The corresponding tensor-product space is denoted by $\mathcal{H}_t\otimes\mathcal{H}_s\otimes\mathcal{H}_p$. In our setup, we have access to those three subspaces: the transversal amplitude space $\mathcal{H}_t$, whose members are transversal functions $\psi(x,y)$ that describe the beam's profile; the polarization space $\mathcal{H}_s$ with basis $\{|H\rangle,|V\rangle\}$; and the path space $\mathcal{H}_p$, with basis $\{|0\rangle,|1\rangle\}$. By submitting a horizontally polarized state $|H\rangle$ to the action of a quarter-wave plate (QWP) and a half-wave plate (HWP), any desired, initial polarization state $|i\rangle$ can be produced. This is the pre-selected state. On submitting $|i\rangle$ to a polarizing beam splitter (PBS), its $|H\rangle$ component goes unaffected through the PBS, while the $|V\rangle$ component is reflected. If we denote by $|0\rangle$ the path along which $|i\rangle$ propagates, and by $|1\rangle$ the path followed by the reflected beam, the PBS performs the map $|H\rangle|0\rangle\to|H\rangle|0\rangle$, $|V\rangle|0\rangle\to|V\rangle|1\rangle$. The action of the PBS is represented by the unitary and self-adjoint operator

$$U_{\rm PBS} = U^{\dagger}_{\rm PBS} = \mathbb{1}_t\otimes\left(\widehat{\Pi}_H\otimes\mathbb{1}_p + \widehat{\Pi}_V\otimes\sigma^x_p\right), \tag{12}$$

where $\widehat{\Pi}_H = |H\rangle\langle H|$, $\widehat{\Pi}_V = |V\rangle\langle V|$, $\sigma^x_p = |0\rangle\langle 1| + |1\rangle\langle 0|$, while $\mathbb{1}_t$ and $\mathbb{1}_p$ stand for identity operators on transversal amplitude space and path space, respectively.

Our setup implements von Neumann's model of the measurement process. It was designed so that the system-pointer coupling strength is not restricted to have small values [38]. Generally, during the measurement process, the dynamical evolution of system and pointer is ruled by the Hamiltonian $\hat{H} = g\hat{A}\otimes\hat{P}$. We may take $\hat{P}$ to be an impulse operator, with $[\hat{X},\hat{P}] = i\hbar$, where $\hat{X}$ is the position operator that fixes the pointer's readout. The system-pointer evolution is given by the unitary $\hat{U}(\epsilon) = \exp(-i\epsilon\hat{A}\otimes\hat{P}/\hbar)$, where $\epsilon = g\tau$ and τ is a pulse-like interaction time. WVs were originally introduced [1] under the assumption of weak coupling strengths (weak measurements), so that ϵ is very small and one may perform a Taylor series expansion up to first order: $\hat{U}(\epsilon)\approx\mathbb{1} - i\epsilon\hat{A}\otimes\hat{P}/\hbar$. Various results, among them those of [32, 33], were derived under this assumption. In our case, we resort to closed-form expressions, valid to all orders of ϵ [39–41].

We are specially interested in two-state systems, and more specifically, on polarization. An example of a system operator in this case is

$$\hat{A} = \mathbf{n}\cdot\boldsymbol{\sigma}\equiv\hat{\sigma}_n. \tag{13}$$

Here, $\mathbf{n}$ is a unit vector and $\boldsymbol{\sigma} = (\sigma_1,\sigma_2,\sigma_3)$ is the triple of Pauli matrices. The basis vectors $|H\rangle$ and $|V\rangle$ are taken to be the eigenvectors of the Pauli matrix σ_1; that is, $\sigma_1 = |H\rangle\langle H| - |V\rangle\langle V|$. As pre-selected system-pointer state $|i\rangle|\psi\rangle$, we take

$$|i\rangle = \cos(\alpha/2)\,|H\rangle + e^{i\beta}\sin(\alpha/2)\,|V\rangle, \qquad \psi(x) = \langle x|\psi\rangle = \frac{1}{(2\pi\sigma^2)^{1/4}}\exp\left(-\frac{x^2}{4\sigma^2}\right). \tag{14}$$

We thus assume that, initially, the pointer's position has a Gaussian distribution $\psi(x)$. This distribution is shifted by the system-pointer coupling. On measuring this shift, one can assign a value to the measured observable. In the present case, there are two possible shifts: $\psi(x)\to\psi(x\pm\epsilon)$, which correspond to the

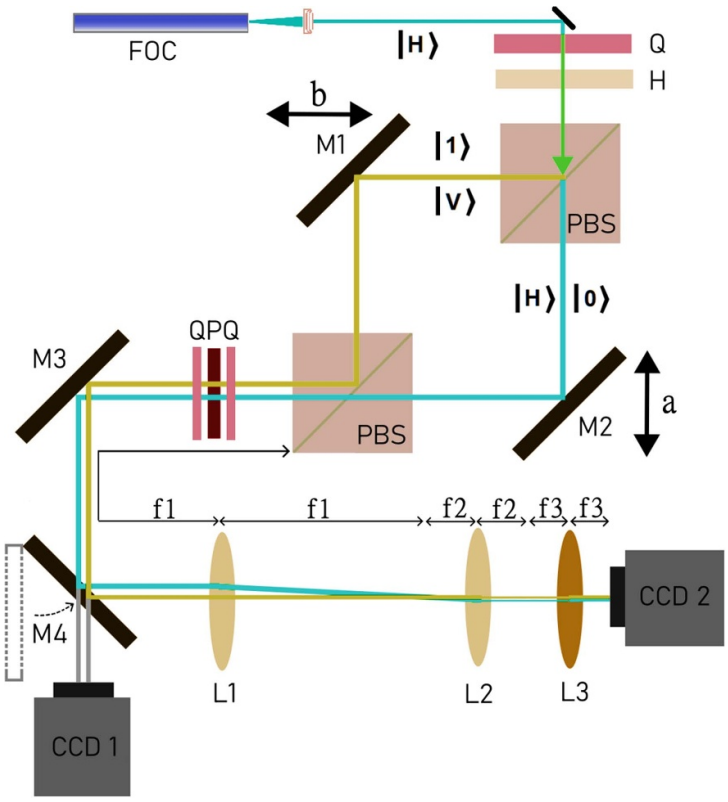

Figure 1. Experimental setup. A laser beam is collected by a monomode optical fiber (FOC) and coupled to a collimator to be horizontally polarized. The pre-selected polarization state $|i\rangle$ is prepared with a QWP and a HWP. The Mach–Zehnder (MZ) setup has two movable mirrors, M_1 and M_2, which can be displaced by distances b and a, respectively. After the MZ, a polarizer P and two QWPs project on the post-selected state $|f\rangle$. The CCD1 camera measures in position space, when mirror M4 is removed. Lenses L_1 and L_2 conform a telescope system that serves to optimize image recording at CCD2. Lens $L3$ performs a Fourier transformation of the transversal amplitude.

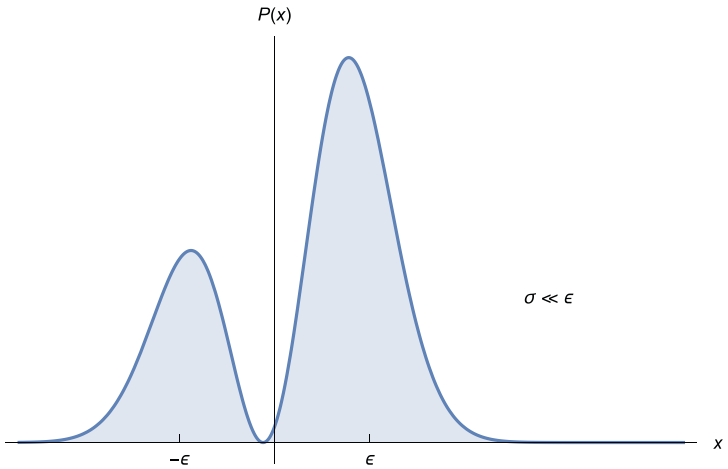

Figure 2. Gaussian distributions in the strong coupling regime, in which the pointer spread (σ) is much smaller than the pointer's shift (ϵ). The two eigenvalues of the measured observable can then be unambiguously correlated with the two well-discernible Gaussian peaks.

eigenvalues ± 1 of $\hat{\sigma}_n$. In the weak coupling regime ($\epsilon \ll \sigma$), there is some overlap between the Gaussian distributions $\psi(x \pm \epsilon)$. To assign a value to $\hat{\sigma}_n$, one must repeat the measurement many times [42]. If $\epsilon \gg \sigma$, one has strong, projective measurements, which allow to unambiguously assign a value to $\hat{\sigma}_n$ (see figure 2). Alternatively, on considering that $\hat{\sigma}_n$ couples to the position operator $\hat{X}$, the shift occurs in $\tilde{\psi}(p) = \langle p|\psi\rangle$, the Fourier transform of $\psi(x)$. In our case, the post-selected pointer-state can be recorded with a charge coupled device (CCD) camera. The image corresponds to position $|x\rangle$ or momentum $|p\rangle$, depending on which CCD camera we use, CCD1 or CCD2 (see figure 1), to record the transversal profile.

As shown in figure 1, the interferometer has two displaceable mirrors, set on the 0 and 1 arms. They shift the transverse amplitude distribution $\psi(x,y)$ along the x-axis and leave unchanged the distribution along the y-axis. That is, $\psi(x,y) \to \psi(x+a,y)$ on the 0-arm, and $\psi(x,y) \to \psi(x+b,y)$ on the 1-arm. The unitary operator, which produces these actions on the amplitude-path subspace, is given by

$$U_{ab} = \exp\left(-\mathrm{i}a\hat{p}_x/\hbar\right) \otimes \widehat{\Pi}_0 + \exp\left(-\mathrm{i}b\hat{p}_x/\hbar\right) \otimes \widehat{\Pi}_1, \tag{15}$$

where $\widehat{\Pi}_k = |k\rangle\langle k|$, $k = 0, 1$ and $\hat{p}_x = -i\hbar\partial_x$ is the impulse operator. That is, $\exp\left(\mathrm{i}a\hat{p}_x/\hbar\right)\psi(x,y) = \psi(x+a,y)$. The displacement by a in the transverse function is thus conditioned on the light-beam going along path $|0\rangle$, and the displacement by b is conditioned on the beam going along path $|1\rangle$. Due to the PBS (see equation (12)), the displacements become effectively connected with the $|H\rangle$ and $|V\rangle$ components, respectively, of the beam polarization. As far as polarization is concerned, we could thus replace in equation (15) $\widehat{\Pi}_0$ by $\widehat{\Pi}_H$ and $\widehat{\Pi}_1$ by $\widehat{\Pi}_V$. Such an U_{ab} would describe the action of a birefringent crystal that is used as polarizing beam displacer. Our setup was designed so as to obtain the same effect, but without the restrictions that derive from using a birefringent crystal, in particular the restriction of having access to only small system-coupling strengths, due to the small beam displacements within the crystal.

As can be seen in figure 1, the core of our setup is the Mach–Zehnder (MZ)-like interferometer with the two moveable mirrors and two PBSs. The total action of this interferometer is given by

$$U_T = U_{\mathrm{PBS}}\left(\mathbb{1}_s \otimes U_{ab}\right) U_{\mathrm{PBS}} \tag{16}$$

$$= \mathrm{e}^{-\mathrm{i}a\hat{p}_x/\hbar} \otimes \left(\widehat{\Pi}_H \otimes \widehat{\Pi}_0 + \widehat{\Pi}_V \otimes \widehat{\Pi}_1\right) + \mathrm{e}^{-\mathrm{i}b\hat{p}_x/\hbar} \otimes \left(\widehat{\Pi}_H \otimes \widehat{\Pi}_1 + \widehat{\Pi}_V \otimes \widehat{\Pi}_0\right). \tag{17}$$

Let us take $|\psi\rangle|i\rangle|0\rangle$ as the pre-selected state, i.e. a polarized state $|i\rangle$ with transversal amplitude $|\psi\rangle$ that propagates along path $|0\rangle$. The post-selected state is $|x\rangle|f\rangle|0\rangle$. We get then the following expression, which involves WVs:

$$\frac{\langle 0|\langle f|\langle x|U_T|\psi\rangle|i\rangle|0\rangle}{\langle f|i\rangle} = \psi(x-a)\,\Pi_H^w + \psi(x-b)\,\Pi_V^w. \tag{18}$$

We stress that equation (18) is not restricted to small displacements. It holds for arbitrary values of a and b. Assuming Gaussian distributions (see (14)), we have

$$\frac{\langle 0|\langle f|\langle x|U_T|\psi\rangle|i\rangle|0\rangle}{\langle f|i\rangle} = \frac{1}{(2\pi)^{1/4}\sqrt{\sigma}}\left\{\exp\left(-\frac{(x-a)^2}{4\sigma^2}\right)\Pi_H^w + \exp\left(-\frac{(x-b)^2}{4\sigma^2}\right)\Pi_V^w\right\}. \tag{19}$$

The corresponding normalized detection probability (intensity in the case of classical light beams) is given by

$$\frac{P_{ab}}{P} = \frac{|\langle f|\langle x|U_T|\psi\rangle|i\rangle|^2}{|\langle f|i\rangle|^2}$$

$$= \frac{1}{\sqrt{2\pi}\sigma}\left\{\exp\left(-\frac{(x-a)^2}{2\sigma^2}\right)|\Pi_H^w|^2 + \exp\left(-\frac{(x-b)^2}{2\sigma^2}\right)|\Pi_V^w|^2 + 2\mathrm{Re}\left[\exp\left(-\frac{(x-a)^2+(x-b)^2}{4\sigma^2}\right)\Pi_H^w\Pi_V^{w*}\right]\right\}. \tag{20}$$

Based on these results, we can measure geometric phases out of WV measurements. We have envisaged two methods to do this, which we explain in what follows.

2.1. First method

Let us consider the case in which $\sigma \ll |a-b|$, so that we have two non-overlapping Gaussian distributions. In this case, $(a-b)^2/\sigma^2 \gg 1$ and we can accurately determine the center of each Gaussian distribution. We can thus define the measurable quantities (see equation (20))

$$C_a = \left.\frac{P_{ab}}{P}\right|_{x\to a} = \frac{1}{\sqrt{2\pi}\sigma}|\Pi_H^w|^2, \tag{21}$$

$$C_b = \left.\frac{P_{ab}}{P}\right|_{x\to b} = \frac{1}{\sqrt{2\pi}\sigma}|\Pi_V^w|^2. \tag{22}$$

Now, from $\widehat{\Pi}_H + \widehat{\Pi}_V = \mathbb{1}$, it follows that $\Pi_H^w + \Pi_V^w = 1$, whereupon, on writing

$$\Pi_H^w = r\mathrm{e}^{\mathrm{i}\chi}, \tag{23}$$

we have

$$|\Pi_V^w|^2 = |1 - re^{i\chi}|^2 = 1 + r^2 - 2r\cos\chi, \tag{24}$$

$$\mathrm{Re}\left[\Pi_H^w \Pi_V^{w*}\right] = r\cos\chi - r^2. \tag{25}$$

Hence, for $|a-b| \gg \sigma$, we get

$$C_a = \frac{r^2}{\sqrt{2\pi}\sigma}, \tag{26}$$

$$C_b = \frac{1}{\sqrt{2\pi}\sigma}\left(1 + r^2 - 2r\cos\chi\right). \tag{27}$$

We can then express χ in terms of measurable quantities:

$$\cos\chi = \frac{1 + \sigma\sqrt{2\pi}\,(C_a - C_b)}{2\,(2\pi)^{1/4}\,(\sigma\,C_a)^{1/2}}. \tag{28}$$

This allows us to measure the geometric phase χ via WVs. Notice that we have taken

$$\Pi_H^w \equiv \Pi_H^w(i,f) \equiv \frac{\langle f|\widehat{\Pi}_H|i\rangle}{\langle f|i\rangle} = \frac{\langle f|H\rangle\langle H|i\rangle}{\langle f|i\rangle} = re^{i\chi}, \tag{29}$$

so that

$$\chi = \arg\Pi_H^w(i,f) = \triangle(i,H,f). \tag{30}$$

There is no loss of generality involved, when we include $|H\rangle$ as one of the three states that enter χ. What matters is the geodesic triangle that is constructed out of three states on the Poincaré sphere, and there is no restriction involved when taking one of these states as a 'horizontal' one, under proper definition of our reference frame. It is well known that χ equals (minus) half the solid angle of the geodesic triangle with vertices $\hat{S}_i$, $\hat{S}_H$, $\hat{S}_f$, the Stokes unit vectors of the states $|i\rangle$, $|H\rangle$, $|f\rangle$, respectively. As proved by Mukunda and Simon [37],

$$\cos\chi = \frac{1 + \hat{S}_i\cdot\hat{S}_H + \hat{S}_H\cdot\hat{S}_f + \hat{S}_f\cdot\hat{S}_i}{\left[\left(1 + \hat{S}_i\cdot\hat{S}_H + \hat{S}_H\cdot\hat{S}_f + \hat{S}_f\cdot\hat{S}_i\right)^2 + \left(\hat{S}_i\cdot\hat{S}_H\times\hat{S}_f\right)^2\right]^{1/2}}. \tag{31}$$

This is a theoretical value, against which we can compare the measured value of $\cos\chi$, given by equation (28).

2.2. Second method

Alternatively, we can obtain the geometric phase by measuring two 'centroids' of the pointer's Gaussian distributions. As we said before, because of the PBS (see equation (12)), the effective action of the two moveable mirrors in figure 1 can be described by the operator

$$U_{ab} = \exp\left(-ia\hat{p}_x/\hbar\right)\otimes e^{i\phi}\widehat{\Pi}_H + \exp\left(-ib\hat{p}_x/\hbar\right)\otimes\widehat{\Pi}_V, \tag{32}$$

instead of equation (15). From equations (20), (24) and (25), we get

$$\frac{P_{ab}(x)}{P} = \frac{1}{\sqrt{2\pi}\sigma}\left\{\left(\psi_a(x) - \psi_b(x)\right)^2 r^2 + 2r\cos\chi\,\psi_b(x)\left(\psi_a(x) - \psi_b(x)\right) + \psi_b^2(x)\right\}, \tag{33}$$

with

$$\psi_k(x) = \exp\left(-\frac{(x-k)^2}{4\sigma^2}\right). \tag{34}$$

In momentum space, we obtain

$$\frac{\langle p|\langle f|U_{ab}|i\rangle|\psi\rangle}{\langle f|i\rangle} = \langle p|e^{-iap/\hbar}\Pi_H^w|\psi\rangle + \langle p|e^{-ibp/\hbar}\Pi_V^w|\psi\rangle = \tilde{\psi}(p)\left(e^{-iap/\hbar}\Pi_H^w + e^{-ibp/\hbar}\Pi_V^w\right), \tag{35}$$

where $\tilde{\psi}(p)$ is the Fourier transform of $\psi(x)$. On taking the modulus squared of the above expression, we get the normalized probability (intensity):

$$\frac{\widetilde{P}_{ab}(p)}{P} = \frac{|\langle f|\langle p|U_{ab}|\psi\rangle|i\rangle|^2}{|\langle f|i\rangle|^2} = \tilde{\psi}^2(p)\left(|\Pi_H^w|^2 + |\Pi_V^w|^2 + 2\mathrm{Re}\left[e^{2i(a-b)p/\hbar}\Pi_H^w(\Pi_V^w)^*\right]\right)$$
$$= \tilde{\psi}^2(p)\left\{1 + 2r^2 - 2r\cos\chi + 2r\cos(\chi - (a-b)p/\hbar) - r^2\cos((a-b)p/\hbar)\right\} \tag{36}$$

On setting $b = -a$, the centroids in x-space and p-space are given by:

$$C_x = \frac{1}{P}\int_{-\infty}^{\infty} xP_{ab}(x)\,\mathrm{d}x = a(2r\cos\chi - 1), \tag{37}$$

$$C_p = \frac{1}{P}\int_{-\infty}^{\infty} p\widetilde{P}_{ab}(p)\,\mathrm{d}p = \frac{2\sqrt{2\pi}}{\sigma^2 e^{1/\sigma^2}} r\sin\chi. \tag{38}$$

It is then convenient to weight the pixels on the CCD device not with x and p, but with x/a and $\sigma^2 e^{\frac{1}{\sigma^2}}p$, respectively, so that we obtain the normalized centroids:

$$\bar{C}_x = \frac{1}{P}\int_{-\infty}^{\infty} (x/a)\,P_{ab}(x)\,\mathrm{d}x = 2r\cos\chi - 1, \tag{39}$$

$$\bar{C}_p = \frac{1}{P}\int_{-\infty}^{\infty} \left(\sigma^2 e^{\frac{1}{\sigma^2}}p\right)P_{ab}(p)\,\mathrm{d}p = 2\sqrt{2\pi}\,r\sin(\chi). \tag{40}$$

From these normalized centroids, we obtain the following relations:

$$\bar{C}_x + 1 = 2r\cos\chi, \tag{41}$$

$$\frac{1}{\sqrt{2\pi}}\bar{C}_p = 2r\sin\chi. \tag{42}$$

The geometric phase χ is now given by

$$\tan\chi = \frac{\bar{C}_p}{\sqrt{2\pi}(\bar{C}_x + 1)}. \tag{43}$$

In this way, we obtain another expression for χ in terms of experimentally measurable quantities. This result can be compared with the theoretical one [37]:

$$\tan\chi = -\frac{\hat{S}_i\cdot\left(\hat{S}_H\times\hat{S}_f\right)}{1 + \hat{S}_i\cdot\hat{S}_H + \hat{S}_H\cdot\hat{S}_f + \hat{S}_f\cdot\hat{S}_i}. \tag{44}$$

3. Experiments and results

We implemented the two methods for measuring geometric phases that we explained before. Our experimental setup is shown in figure 1. Our light source was a HeNe laser (12.5 mW at 633 nm), which delivered a laser beam that was horizontally polarized and collected by a monomode optical fiber (SM600-Thorlabs, 633–780 nm, 125 μm cladding), coupled to a collimator (CL, Thorlabs FOC: F230FC-B-633 nm, $f = 4.43$ mm, NA = 0.56 FC/PC). Both the pre-selected state $|i\rangle$ and the post-selected state $|f\rangle$ were prepared in essentially the same way, based on the action of a HWP and a QWP on a horizontally polarized state $|H\rangle$. A general, pre-selected state reads $|i\rangle = \cos(\theta/2) + e^{i\varphi}\sin(\theta/2)$. Its Stokes vector is $\boldsymbol{S}_{|i\rangle} = (\cos\theta, \sin\theta\cos\varphi, \sin\theta\sin\varphi)$. This state should be obtained by submitting $|H\rangle$ to a QWP (Thorlabs WPMQ05M-633) and a HWP (Thorlabs WPMH05M-633). On writing the resulting state as $H(\alpha/4)Q(\beta/2)|H\rangle$, it has the Stokes vector $\boldsymbol{S}_{\mathrm{QH}} = (\cos(\alpha-\beta)\cos\beta, \sin(\alpha-\beta)\cos\beta, \sin\beta)$. We can therefore set

$$\alpha = \arctan(\tan\theta\cos\varphi) + \arcsin(\sin\theta\sin\varphi), \tag{45}$$

$$\beta = \arcsin(\sin\theta\sin\varphi), \tag{46}$$

to obtain the desired state $|i\rangle$. This state is submitted to the MZ interferometer that is part of the setup shown in figure 1. The output beam of this interferometer should be projected on a post-selected state $|f\rangle$, the general form of which is like the one of the pre-selected state $|i\rangle$. We thus need to implement the projector

$|f\rangle\langle f|$. To this end, we proceed as before, but permuting the order in which the QWP and the HWP act on $|H\rangle$. On using $H(\alpha/4)Q(\beta/2) = Q((\alpha-\beta)/2)H(\alpha/4)$, we have

$$\begin{aligned} |f\rangle\langle f| &= Q\left(\frac{\alpha-\beta}{2}\right)H\left(\frac{\alpha}{4}\right)|H\rangle\langle H|H^{\dagger}\left(\frac{\alpha}{4}\right)Q^{\dagger}\left(\frac{\alpha-\beta}{2}\right) \\ &\equiv Q\left(\frac{\alpha-\beta}{2}\right)P\left(\frac{\alpha}{2}\right)Q^{\dagger}\left(\frac{\alpha-\beta}{2}\right) = Q\left(\frac{\alpha-\beta}{2}\right)P\left(\frac{\alpha}{2}\right)Q\left(\frac{\alpha-\beta+\pi}{2}\right), \end{aligned} \tag{47}$$

where $P(\alpha/2) = |\alpha/2\rangle\langle\alpha/2|$ corresponds to a polarizer set to $\alpha/2$, i.e. a projector on the linearly polarized state $|\alpha/2\rangle = H(\alpha/4)|H\rangle = \cos(\alpha/2)|H\rangle + \sin(\alpha/2)|V\rangle$. On choosing α and β as given by equations (45) and (46), equation (47) represents a general projector (filter) $|f\rangle\langle f|$, which is made with two QWPs and a polarizer [43].

We performed measurements in both position space and momentum space, as required by the two proposed methods. This required calibrating the phase ϕ, by setting the displacement a of the corresponding moveable mirror, to $a = n\lambda$, with n integer. In this way, we have $\phi = 0 \mod (2\pi)$. We fixed a with the help of the CCD1 camera (DCU223C, 1024×768 resolution, 4.65 μm pixel size) shown in figure 1, by measuring the relative positions of the centroids of horizontally and vertically polarized beams. We obtained $a = 2370\,\lambda \approx 1.50 \pm 0.03$ mm, which corresponds to $n = 2370 \pm 47$.

The actual implementation of the methods explained in sections 2.1 and 2.2 involved two-dimensional images that were recorded in the CCD cameras. Hence, some slight modifications of the theoretical results given above are necessary, in order to describe our experimental outputs. To begin with, the preselected state now reads

$$|\psi_{\rm in}\rangle = |\psi\rangle|i\rangle|0\rangle, \text{ with } \quad \psi(x,y) = \langle x,y|\psi\rangle = \sqrt{\frac{1}{2\pi\,\sigma_{\omega}^{2}}}\exp\left(-\frac{x^{2}+y^{2}}{4\sigma_{\omega}^{2}}\right). \tag{48}$$

Transverse profiles must be measured in position space and in momentum space. The latter requires submitting the profile to a Fourier transformation, something that can simply be done with a lens. Let us consider two transverse profiles, one of which, ψ, is at the focal distance f before the lens, while the other, ψ', is at distance f after the lens. These profiles are related by [44]

$$\psi(x,y) \underset{\text{lens}}{\longrightarrow} \frac{1}{\lambda f}\int\int \psi(x,y)\,\mathrm{e}^{\mathrm{i}2\pi x\nu_x}\mathrm{e}^{\mathrm{i}2\pi y\nu_y}\mathrm{d}x\mathrm{d}y \equiv \frac{1}{\lambda f}\mathcal{F}\{\psi\}(\nu_x,\nu_y) \equiv \psi'(x',y'), \tag{49}$$

where the equalities $x' = \lambda f\nu_x$ and $y' = \lambda f\nu_y$ connect the (spatial) frequencies (ν_x,ν_y) with the position coordinates (x',y') on the output plane.

Even though one Fourier lens suffices to obtain the profile in momentum space, in practice it was necessary to mount a telescopic arrangement with three lenses, L_1, L_2 and L_3, whose focal distances were $f_1 = 250$ mm, $f_2 = 45$ mm and $f_3 = 300$ mm. (see figure 1). The reason was that the transversal profile, which is captured by the CCD camera, should cover a rather large number of pixels, so as to attain the required image resolution. Lenses L_1 and L_2 were used to reduce the spot at the output of the MZ interferometer, so that the third lens L_3 could perform a Fourier transformation with the required resolution in the CCD camera. The locations of the lenses were chosen so that the sum of their focal distances covered the total distance from the output PBS to the CCD camera (see figure 1). In this way, no unwanted phase factors appear in the Fourier transformations [44]. We have then the following relationship between the transversal profiles at the planes before and after the lenses:

$$\psi(x,y) \underset{\text{lenses}}{\longrightarrow} \psi^{(l)}(x',y') = \left(\frac{1}{\lambda f_3 f_2 f_1}\right)\mathcal{F}\left\{\mathcal{F}\left\{\mathcal{F}\{\psi\}\left(\frac{x'''}{\lambda f_1},\frac{y'''}{\lambda f_1}\right)\right\}\left(\frac{x''}{\lambda f_2},\frac{y''}{\lambda f_2}\right)\right\}\left(\frac{x'}{\lambda f_3},\frac{y'}{\lambda f_3}\right). \tag{50}$$

3.1. First method: experimental implementation

As we said before, on account of the two-dimensional nature of the transversal profiles that we record in the experimental implementation, the results previously obtained in section 2.1 must be slightly modified. We recall that we need to have two well resolved Gaussians in position space: $(a-b)^2/\sigma_w^2 \gg 1$. In this case, on using equation (48) we obtain (in place of equations (20), (26) and (27))

$$\frac{P_{ab}(x,y)}{P} = \frac{\mathrm{e}^{-y^2/4\sigma_w^2}}{2\pi\sigma_w^2}\left(\mathrm{e}^{-(x-a)^2/4\sigma_w^2}|\Pi_H^w|^2 + \mathrm{e}^{-(x-b)^2/4\sigma_w^2}|\Pi_V^w|^2 + 2\mathrm{Re}\left[\mathrm{e}^{-\left((x-a)^2+(x-b)^2\right)/4\sigma_w^2}\Pi_H^w\Pi_V^{w*}\right]\right), \tag{51}$$

Table 1. Pre-selected ($|i\rangle$) and post-selected ($|f\rangle$) states are parameterized as $|\psi\rangle = \cos(\alpha/2)|H\rangle + e^{i\beta}\sin(\alpha/2)|V\rangle$. Each of the 4 curves shown in figure 3 is a geodesic triangle, whose vertices are the states $|i\rangle$, $|H\rangle$ and $|f\rangle$.

Curve Nr.	α_i	β_i	α_f	β_f
1	64.3°	33.7°	90.0°	180.0°
2	90.0°	90.0°	90.0°	180.0°
3	90.0°	180.0°	120.0°	125.3°
4	90.0°	0.0°	60.0°	−54.74°

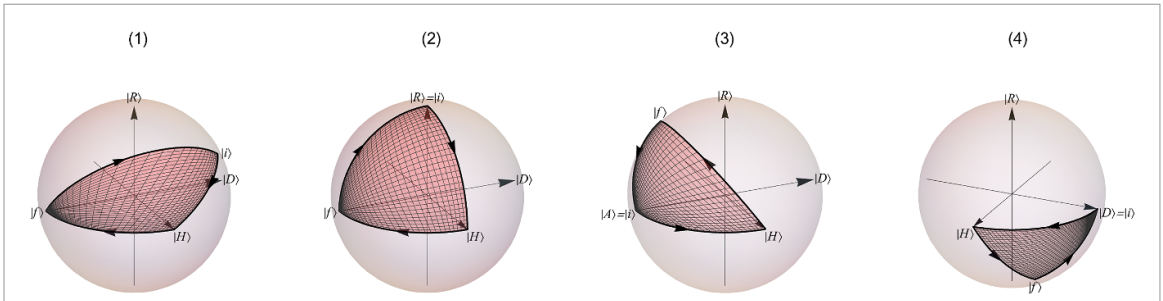

Figure 3. Geodesic arcs connect the states $|i\rangle, |H\rangle$ and $|f\rangle$. The resulting geodesic triangle subtends a solid angle Ω, such that the geometric phase $\chi = -\Omega/2$.

$$C_a = \frac{P_{\rm ab}}{P}\bigg|_{x\to a, y\to 0} = |\Pi_H^w|^2 = \frac{1}{2\pi\sigma_w^2} r^2, \tag{52}$$

$$C_b = \frac{P_{\rm ab}}{P}\bigg|_{x\to b, y\to 0} = |\Pi_V^w|^2 = \frac{1}{2\pi\sigma_w^2}\left(1 + r^2 - 2r\cos\chi\right). \tag{53}$$

From the above equations, we get

$$\cos\chi = \frac{1 + 2\pi\sigma_w^2 (C_a - C_b)}{2\sqrt{2\pi\sigma_w^2 C_a}}. \tag{54}$$

To record the required images in position space, we used the CCD1 camera, see figure 1. We chose $a = 2.00 \pm 0.02$ mm, which corresponds to $n\lambda$, with $n = 3158 \pm 29$. We prepared 4 pairs of pre-selected (i) and post-selected (f) polarization states of the form $|\psi\rangle = \cos(\alpha/2) + e^{i\beta}\sin(\alpha/2)$, with the α, β given in table 1. Figure 3 shows the surface enclosed by the geodesic arcs that connect the states $|i\rangle$, $|H\rangle$ and $|f\rangle$, in the 4 cases. Each surface subtends a solid angle Ω, which is related to the geometric phase by $\chi = -\Omega/2$ [37].

For each pair of pre-selected and post-selected states, we recorded 15 images and, in each case, we repeated the measurement 5 times. To determine the maximal peak intensity, we adjusted the recorded profiles to Gaussian distributions, see figure 4. The goodness of fit, i.e. the R-squared values, are shown in table 2 for the left and right spots on the CCD camera. As can be seen, in all cases the Gaussian fit contained more than 90% of the data. The measured value of σ_ω was 0.49 ± 0.03 mm. The experimental values we obtained for the geometric phase χ, given by $\cos\chi$, are shown in figure 5. As can be seen, the experimental values that were obtained from the measured quantities entering equation (54) are in good agreement with the theoretical ones that follow from equation (31).

3.2. Second method: experimental implementation

The second method requires the field amplitude in momentum space, $\psi^{(l)}(x,y)$, which is the Fourier transform of the field amplitude in position space (see equation (50)). We thus record the images of the transversal profile on the CCD2 camera (see figure 1), with the array of three lenses set on place. The geometric phase χ that is associated to each geodesic triangle is now given by $\tan\chi$. The experimental value of the latter can be expressed in terms of measurable quantities, as follows.

On using the Fourier transformed, transversal profile $\psi^{(l)}(x,y)$, we get the following results:

$$\frac{P_{\rm ab}^{(l)}(x,y)}{P} = |\psi_a^2(x,y)|^2\left(1 + 2r^2 - 2r\left(r\cos(\phi + \phi_l) + \cos\chi - \cos(\chi + \phi + \phi_l)\right)\right), \tag{55}$$

$$C_x = \int x\frac{P_{ab}(x,y)}{P}\,dxdy = -\frac{a}{2}(2r\cos\chi - 1), \tag{56}$$

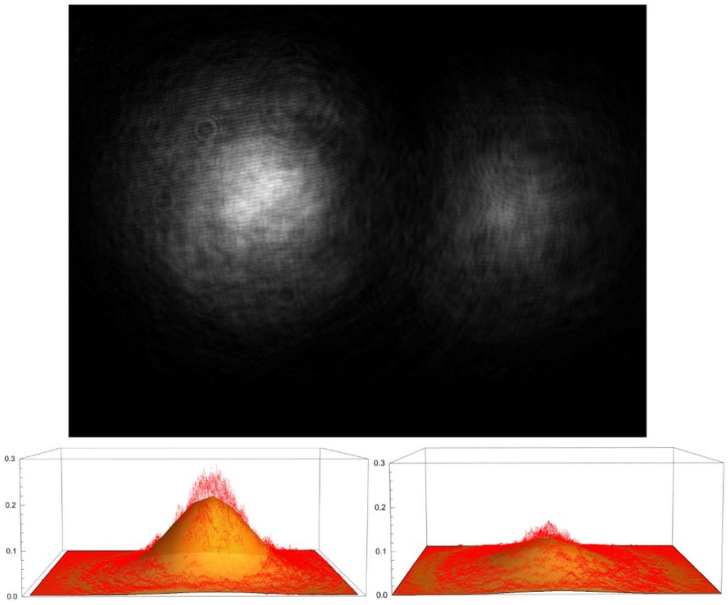

Figure 4. Spots on the CCD camera and their Gaussian fits.

Table 2. R^2 for the Gaussian fits of the left and right spots on the CCD camera. Curve numbers refer to the geodesic triangles in figure 3.

Curve Nr.	R^2 (left)	R^2 (right)
1	0.96	0.95
2	0.94	0.95
3	0.91	0.95
4	0.94	0.91

$$C_p = \int x \frac{P_{ab}^{(l)}(x,y)}{P} \mathrm{d}x\mathrm{d}y = -\frac{a\mathrm{e}^{-a^2/8\sigma_w^2} f_1 f_3 r\lambda}{4\pi f_2 \sigma_w^2} \sin\chi, \tag{57}$$

where we have set $\phi_l = \arg[\psi_a^{(l)}(x,y)\psi_b^{(l)}(x,y)]$. The above results are an extension of equations (36)–(38), valid for the two-dimensional case. From these results, we get

$$\tan\chi = \frac{8\pi\sigma_w^2 f_2 \mathrm{e}^{a^2/8\sigma_w^2} C_p}{\lambda f_1 f_3} \left(\frac{C_p}{2C_x - a}\right). \tag{58}$$

The aforementioned array of three lenses was aligned so that the vertically polarized beam coincided with the optical axis. Our reference point on the CCD camera was the position of the centroid of the vertically polarized beam $|V\rangle$. We adjusted the relative phase so that $\phi = 0, \mathrm{mod}(2\pi)$ and recorded 15 images of the beam's transversal profile for each pre-selected state, repeating the process 5 times in each case. We measured the centroids' positions relative to the reference point and took their average, which is given by $C_p P/A_x$, with $A_x = \int P_{ab}(x,y)\mathrm{d}x\mathrm{d}y$. From this average, we got C_p. As for C_x, it proved convenient to fix as reference point on the CCD camera the middle point between the centroids of the $|V\rangle$ and $|H\rangle$ beams. We recorded 15 images and repeated the process 5 times in each case and obtained an average value $C_x P/A_x$. In the two cases, P was obtained by just measuring the intensity of the beam that resulted from preparing the pre-selected state $|i\rangle$ with a QWP and a HWP, as explained before, followed by the projection on the post-selected state $|f\rangle$. This projection was done with two QWPs and a polarizer, as already explained. In this way, we measured P for each pair of pre-selected and post-selected states. Figure 6 shows the measured values of $\tan\chi$ (solid bars) and the theoretical values (dashed bars). The corresponding numerical values of $\tan\chi$ are given in table 3. Here again, experimental and theoretical values are in good agreement.

Finally, it is worth comparing our approach with another one, which is also based on the three-vertex Bargmann invariant [45]. Although the experimental setup of the latter markedly differs from ours and is unrelated to WVs, the two approaches have the common feature that neither state evolution nor elimination of the dynamical phase are required. In spite of the fact that the experimental results of [45] correspond to a rather limited set of polarized states—which are characterized by a single parameter—a shared advantage of

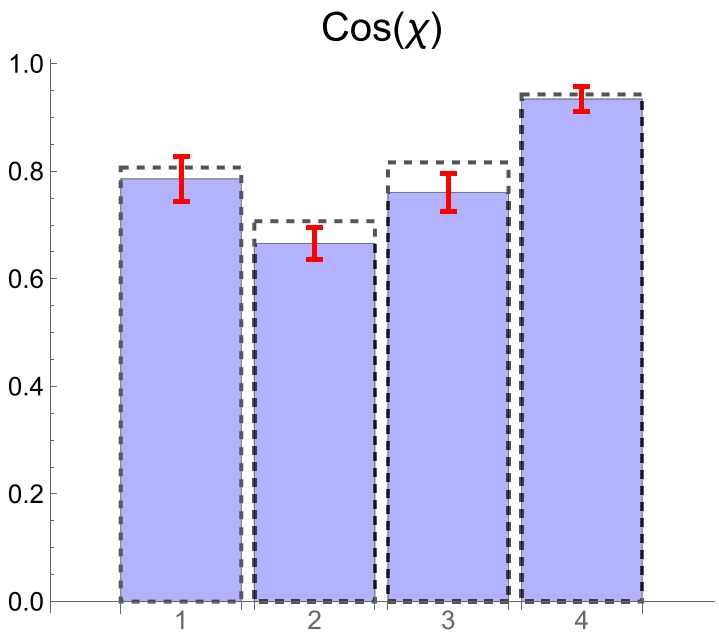

Figure 5. Solid bars correspond to $\cos\chi$, as measured by the first method. Dashed bars are theoretical values. Numbers on the abscissa-axis refer to the geodesic triangles in figure 3.

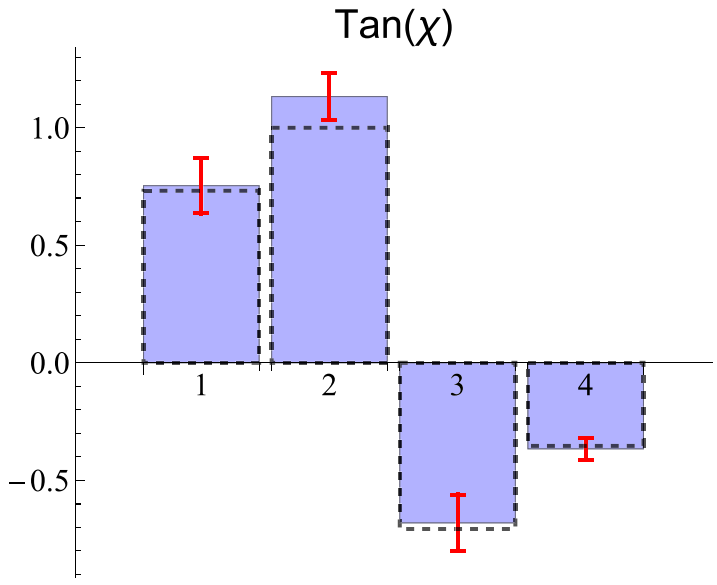

Figure 6. Solid bars represent values of $\tan\chi$, as measured by the second method (see text). Dashed bars are theoretical values. Numbers on the abscissa-axis refer to the geodesic triangles in figure 3.

Table 3. Experimental and theoretical values of $\tan\chi$. Curve numbers refer to the geodesic triangles in figure 3.

Curve Nr.	$\tan\chi$ (theo.)	$\tan\chi$ (exp.)
1	0.73	0.75 ± 0.12
2	1.00	1.13 ± 0.10
3	-0.71	-0.68 ± 0.12
4	-0.35	-0.37 ± 0.05

the two approaches is that all the information is contained in single-shot images of a CCD camera. The setup of [45] uses a three-pinhole interferometer, whose construction requires a rather cumbersome procedure: the accurate perforation and subsequent positioning of a thin copper foil. On the other hand, the setup of [45] does not require phase calibration, as in our case. There is therefore some trade-off to be made, according to

the particular goals one has in mind. We have limited ourselves to address geodesic triangles for the proof-of-concept that we report in this work. Any other curve C may be approximated by some finite number of geodesic arcs, for which equation (10) holds and hence our method applies. Of course, a proper automation must be implemented in order to get the geometric phase that is associated to C (see equation (6)). C may be closed or open. If C is open, it can be completed to a closed curve with a geodesic arc connecting the final and the initial points of C. The geometric phases of the open and closed curves are the same. This is so, because the geometric phase of a geodesic arc is zero [37]. One can envision an extension of our work to address curves that are more or less arbitrary. Similar considerations hold for sequential WV measurements with varying strengths [46]. Another possible extension of our work could come from addressing the question as to whether our results conform the restrictions imposed by so-called weak quantum evolutions [47].

4. Closing remarks

We have proposed and implemented two methods for measuring geometric phases via WVs. Our methods overcome the restrictions imposed by the weak coupling regime between system and measuring device that is usually assumed when dealing with WVs. We used a classical light source to perform our experiments. All the measured quantities were light intensities. We have shown that these intensities contain phase information, out of which one can determine geometric phases. The same holds for probabilities in the case of single photons, to which our methods apply with just minor modifications. Our proof-of-concept shows that geometric phases and WVs are essential features that are not restricted to the quantum domain, even though they were originally identified in that domain. What is essential in the two cases is the linear vector space structure, in terms of which one describes the physical phenomena that are involved in these cases.

Data availability statement

All data that support the findings of this study are included within the article (and any supplementary files).

Acknowledgments

This work was partially supported by the European Union, Project IPN-Bio (reference: H2020-MSCA-RISE-2019-872049), and by the Generalitat Valenciana of Spain (reference: CIPROM/2022/30).

ORCID iDs

C Montenegro https://orcid.org/0000-0002-4661-8231
F De Zela https://orcid.org/0000-0002-3757-1769

References

[1] Aharonov Y, Albert D Z and Vaidman L 1988 How the result of a measurement of a component of the spin of a spin-1/2 particle can turn out to be 100 *Phys. Rev. Lett.* **60** 1351
[2] Berry M V 1984 Quantal phase factors accompanying adiabatic changes *Proc. R. Soc.* A **392** 45
[3] Tomita A and Chiao R Y 1986 Observation of Berry's topological phase by use of an optical fiber *Phys. Rev. Lett.* **57** 937
[4] Ritchie N W M, Story J G and Hulet R G 1991 Realization of a measurement of a 'Weak Value' *Phys. Rev. Lett.* **66** 1107
[5] Spreeuw R J C 1998 A classical analogy of entanglement *Found. Phys.* **28** 361–74
[6] Borges C V S, Hor-Meyll M, Huguenin J A O and Khoury A Z 2010 Bell-like inequality for the spin-orbit separability of a laser beam *Phys. Rev.* A **82** 033833
[7] Qian X-F and Eberly J H 2011 Entanglement and classical polarization states *Opt. Lett.* **36** 4110
[8] Kagalwala K H, Di Giuseppe G, Abouraddy A F and Saleh E A 2013 Bell's measure in classical optical coherence *Nat. Photon.* **7** 72
[9] Qian X-F, Little B, Howell J C and Eberly J H 2015 Shifting the quantum-classical boundary: theory and experiment for statistically classical optical fields *Optica* **2** 611
[10] Aiello A, Töppel F, Marquardt C, Giacobino E and Leuchs G 2015 Quantum-like nonseparable structures in optical beams *New J. Phys.* **17** 043024
[11] McLaren M, Konrad T and Forbes A 2015 Measuring the nonseparability of vector vortex beams *Phys. Rev.* A **92** 023833
[12] Ndagano B *et al* 2017 Characterizing quantum channels with nonseparable states of classical light *Nat. Phys.* **13** 397
[13] Al-Qasimi A 2020 Coherence, entanglement and complementarity in mixed classical light *J. Opt. Soc. Am.* A **37** 1526
[14] Qureshi T 2021 Predictability distinguishability and entanglement *Opt. Lett.* **46** 492
[15] Duck I M, Stevenson P M and Sudarshan E C G 1989 The sense in which a 'weak measurement' of a spin-1/2 particle's spin component yields a value 100 *Phys. Rev.* D **40** 2112
[16] Leggett A J 1989 Comment on 'How the result of a measurement of a component of the spin of a spin-1/2 particle can turn out to be 100' *Phys. Rev. Lett.* **62** 2325
[17] Peres A 1989 Quantum measurements with postselection *Phys. Rev. Lett.* **62** 2326

[18] Aharonov Y and Vaidman L 1989 Aharonov and Vaidman reply *Phys. Rev. Lett.* **62** 2327
[19] Aharonov Y and Vaidman L 1990 Properties of a quantum system during the time interval between two measurements *Phys. Rev.* A **41** 11–20
[20] Dressel J, Malik M, Miatto F M, Jordan A N and Boyd R W 2014 Colloquium: understanding quantum weak values: basics and applications *Rev. Mod. Phys.* **86** 307
[21] Hosten O and Kwiat P 2008 Observation of the spin-Hall effect of light via weak measurements *Science* **319** 787
[22] Kocsis S, Braverman B, Ravets S, Stevens M J, Mirin R P, Shalm L K and Steinberg A M 2011 Observing the average trajectories of single photons in a two-slit interferometer *Science* **332** 1170
[23] Lundeen J S, Sutherland B, Patel A, Stewart C and Bamber C 2011 Direct measurement of the quantum wavefunction *Nature* **474** 188
[24] Groen J P, Riste D, Tornberg L, Cramer J, de Groot P C, Picot T, Johansson G and DiCarlo L 2013 Partial-measurement backaction and nonclassical weak values in a superconducting circuit *Phys. Rev. Lett.* **111** 090506
[25] Salvail J Z, Agnew M, Johnson A S, Bolduc E, Leach J and Boyd R W 2013 Full characterization of polarization states of light via direct measurement *Nat. Photon.* **7** 316
[26] Kobayashi H, Nonaka K and Shikano Y 2014 Stereographical visualization of a polarization state using weak measurements with an optical-vortex beam *Phys. Rev.* A **89** 053816
[27] Mahler D H, Rozema L, Fisher K, Vermeyden L, Resch K J, Wiseman H M and Steinberg A 2016 Experimental nonlocal and surreal Bohmian trajectories *Sci. Adv.* **2** e1501466
[28] Hariri A, Curic D, Giner L and Lundeen J S 2019 Experimental simultaneous readout of the real and imaginary parts of the weak value *Phys. Rev.* A **100** 032119
[29] Xu L *et al* 2024 Resource-efficient direct characterization of general density matrix *Phys. Rev. Lett.* **132** 030201
[30] Xu L *et al* 2021 Direct characterization of coherence of quantum detectors by sequential measurements *Adv. Phot.* **3** 066001
[31] Xu L *et al* 2021 Direct characterization of quantum measurements using weak values *Phys. Rev. Lett.* **127** 180401
[32] Sjöqvist E 2006 Geometric phase in weak measurements *Phys. Lett.* A **359** 187
[33] Tamate S, Kobayashi H, Nakanishi T, Sugiyama K and Kitano M 2009 Geometrical aspects of weak measurements and quantum erasers *New J. Phys.* **11** 093025
[34] Wagh A G and Rakhecha V C 1995 On measuring the Pancharatnam phase. I. Interferometry *Phys. Lett.* A **197** 107
[35] Wagh A G and Rakhecha V C 1995 On measuring the Pancharatnam phase. II. SU(2) Polarimetry *Phys. Lett.* A **197** 112
[36] Bargmann V 1964 Note on Wigner's theorem on symmetry operations *J. Math. Phys.* **5** 862
[37] Mukunda N and Simon R 1993 Quantum kinematic approach to the geometric phase I. General formalism, Ann. Phys., N. Y. **228** 205
[38] Montenegro C, Jara M, Marrou J P and De Zela F 2024 Stokes vector characterization by stronlgy measuring weak values *J. Opt. Soc. Am.* A **41** 723
[39] Denkmayr T, Geppert H, Lemmel H, Waegell M, Dressel J, Hasegawa Y and Sponar S 2017 Experimental demonstration of direct path state characterization by strongly measuring weak values in a matter-wave interferometer *Phys. Rev. Lett.* **118** 010402
[40] Calderaro L, Foletto G, Dequal D, Villoresi P and Vallone G 2018 Direct reconstrucion of the quantum density matrix by strong measurements *Phys. Rev. Lett.* **121** 230501
[41] De Zela F 2022 Role of weak values in strong measurements *Phys. Rev.* A **105** 042202
[42] Pryde G J, O'Brien J L, White A G, Ralph T C and Wiseman H M 2005 Measurement of quantum weak values of photon polarization *Phys. Rev. Lett.* **94** 220405
[43] Simmons J W and Guttmann M J 1970 States waves and photons: a modern introduction to light (Addison-Wesley Publishing Company)
[44] Saleh B E and Teich M C 2019 *Fundamentals of Photonics* (Wiley)
[45] Kobayashi H, Tamate S, Nakanishi T, Sugiyama K and Kitano M 2010 Direct observation of geometric phases using a three-pinhole interferometer *Phys. Rev.* A **81** 012104
[46] Cho Y-W *et al* 2019 Emergence of the geometric phase from quantum measurement back-action *Nat. Phys.* **15** 665
[47] Skorobagatko G A 2022 Restrictions on the existence of weak values in quantum mechanics: weak quantum evolution concept *Phys. Lett.* A **421** 127770